Intracardiac Echocardiography (ICE) Measurement of Dynamic Myocardial Stiffness with Shear Wave Velocimetry

Peter J. Hollender[a,*], **Patrick D. Wolf**[a], **Robi Goswami**[b], and **Gregg E. Trahey**[a]

[a]Department of Biomedical Engineering, Duke University, Durham, North Carolina

[b]Department of Cardiology, Duke University Medical Center, Durham, North Carolina

Abstract

Acoustic Radiation Force (ARF)-based methods have been demonstrated to be a viable tool for noninvasively estimating tissue elastic properties, and shear wave velocimetry has been used to quantitatively measure the stiffening and relaxation of myocardial tissue in open-chest experiments. Dynamic stiffness metrics may prove to be indicators for certain cardiac diseases, but a clinically-viable means of remotely generating and tracking transverse wave propagation in myocardium is needed. Intracardiac echocardiography (ICE) catheter-tip transducers are demonstrated here as a viable tool for making this measurement. ICE probes achieve favorable proximity to the myocardium, enabling the use of shear wave velocimetry from within the right ventricle throughout the cardiac cycle. This work describes the techniques used to overcome the challenges of using a small probe to perform ARF-driven shear wave velocimetry, and presents *in vivo* porcine data showing the effectiveness of this method in the interventricular septum. Acoustic Radiation Force (ARF)-based methods have been demonstrated to be a viable tool for noninvasively estimating tissue elastic properties, and shear wave velocimetry has been used to quantitatively measure the stiffening and relaxation of myocardial tissue in open-chest experiments. Dynamic stiffness metrics may prove to be indicators for certain cardiac diseases, but a clinically-viable means of remotely generating and tracking transverse wave propagation in myocardium is needed. Intracardiac echocardiography (ICE) catheter-tip transducers are demonstrated here as a viable tool for making this measurement. ICE probes achieve favorable proximity to the myocardium, enabling the use of shear wave velocimetry from within the right ventricle throughout the cardiac cycle. This work describes the techniques used to overcome the challenges of using a small probe to perform ARF-driven shear wave velocimetry, and presents *in vivo* porcine data showing the effectiveness of this method in the interventricular septum.

Keywords

*Address Correspondence to: Peter J. Hollender, Department of Biomedical Engineering, Duke University, 136 Hudson Hall Box 90281, Durham, NC 27708, pe-ter.hollender@duke.edu; (919) 660-5422.

Introduction

Various methods have been developed to characterize the beating heart's dynamic elastic properties in the hopes of providing a key indicator of cardiac health and function. Ejection Fraction (EF), for example, is a measurement of the relative change in volume of a heart chamber as it beats; a low EF is often used as an indicator for risk of heart failure. While EF measurements can be made readily and noninvasively with conventional B-mode echocardiography, one study found that in approximately one-third of heart failure cases, EF was normal, though a passive stiffening of the left ventricle was present (Zile et al., 2004). Westermann et al. (2008) also found abnormal relaxation in patients with heart failure and normal EF.

The clinical importance of dynamic myocardial stiffness has been extensively researched, in both the left ventricle (Zile et al., 2004; Westermann et al., 2008) and the right ventricle (Mebazaa et al., 2004; Bleeker et al., 2006; Haddad et al., 2008). Both the absolute stiffness of the myocardium at various points in the cardiac cycle, and contractility, the relative changes in stiffness between systole and diastole, are of interest. Magnetic resonance imaging (MRI) has recently been shown to be able to characterize the elasticity of the left ventricle (LV) through the cardiac cycle with a technique called magnetic resonance elastography (MRE) (Kolipaka et al., 2010). MRE measures the propagation velocity of acoustically-generated mechanical waves across the heart with MRI to determine its elastic properties. While MRE is able to measure global LV stiffness, MRI is expensive and relatively slow, and many patients have conditions or implants precluding them from undergoing MRI, while others may have regional defects that could be missed by these global metrics.

Ultrasonic Measurements of Myocardial Elasticity

Ultrasound may provide a readily available, real-time solution for dynamic cardiac elasticity imaging, as numerous echocardiographic techniques have been proposed to analyze myocardial stiffness and contractility. A quantitative measurement of the dynamic myocardial stiffness may have implications for diagnosing dysfunction as well as characterizing abnormal regions due to infarct or ischemia. Several such ultrasonic techniques are being explored vigorously, including strain and strain-rate imaging (Langeland et al., 2005; D'Hooge et al., 2000; Serri et al., 2006) Acoustic Radiation Force Impulse (ARFI) imaging techniques (Hsu et al., 2007a), and velocimetric methods (Bouchard et al., 2009b; Pislaru et al., 2009; Couade et al., 2011; Pernot et al., 2011; Kanai, 2005). Like MRE, ARFI and velocimetric methods measure the transient mechanical response of tissue to indicate elasticity, but use ultrasound to track and often generate the mechanical waves. Kanai (2005) first imaged the propagation of mechanical Lamb waves from aortic valve closure (AVC) in the interventricular septum (IVS) to estimate viscoelastic properties. Hsu et al. (2007a) first showed a cyclically-varying on-axis ARFI response in open-chest canine myocardium, coupling the transducer to the heart wall to control for motion. Bouchard *et al.* similarly demonstrated the feasibility of using ultrasound to track the velocity of ARF-induced transverse waves in an open-chest experiment for a quantitative measure of elasticity (Bouchard et al., 2009b, 2011), but also noted the challenge that remotely generating displacements in rapidly moving tissue would pose. Pislaru et al. (2009) estimated viscoelastic properties using Lamb wave propagation in the open-chest ovine free wall in response to a coupled mechanical shaker. Couade et al. (2011) also used open-chest preparations to achieve proximity in sheep, and was able to generate and track shear wave propagation in myocardial tissue throughout the cardiac cycle *in vivo* with supersonic shear imaging. Pernot et al. (2011) has recently achieved similar success with supersonic shear imaging, but with a Langendorff *ex vivo* preparation of rat hearts to study the effect of preload pressures on systolic stiffness.

Intracardiac Echocardiography

Pernot et al. (2011) suggest that to perform rapid shear wave velocimetry *in vivo* with clinical viability, a low frequency echocardiography probe would be needed for transthoracic imaging. To date, we have been unable to reliably generate and track transverse waves in myocardium transthoracically, and we propose here an alternative approach to move from open-chested experiments to closed-chested ones, towards clinical applicability. This work demonstrates the feasibility of using Intracardiac Echocardiography (ICE) catheter-tip ultrasonic linear arrays to obtain measures of dynamic myocardial stiffness using shear wave velocimetry. ICE catheters are commonly used echocardiographic tools, providing high-quality images of the heart from within the chambers for assessment of function and guidance of therapy (Mullen et al., 2003; Chu et al., 1994). While a catheterization can be considered at least minimally invasive, in patients with known conditions or those recovering from procedures, the additional information provided to clinicians by elasticity measurements may justify this method for cardiac function monitoring. ICE transducers have already been used for qualitative ARFI imaging *in vivo* (Eyerly et al., 2010; Wolf et al., 2011), though their small size presents a number of challenges, including reactive acoustic force and limited acoustic output, as characterized by Hsu et al. (2007b). By imaging from within the heart chambers, however, proximity to the target tissue is dramatically increased, and acoustic clutter observed in transthoracic echocardiography from the overlying tissue is markedly reduced. *In vivo* data presented here will demonstrate that ICE transducers are capable of making dynamic elasticity measurements similar to those made in open-chest preparations, but in the IVS with minimal invasiveness.

Shear Wave Elasticity Imaging

Shear Wave Elasticity Imaging (SWEI) is a quantitative way to measure tissue elasticity, first proposed by Sarvazyan et al. (1998). Sarvazyan observed that when shear waves are generated in a material, their lateral propagation velocity is determined by their elastic properties. The velocity of propagation of this wave (c_T) is governed under the assumptions of linear behavior in an isotropic, semi-infinite medium by

$$c_T = \sqrt{\frac{\mu}{\rho}}, \quad (1)$$

where μ [kPa] is the shear modulus of elasticity (second Lamé constant) and ρ [kg/m^3] is the density. The assumptions of linearity, isotropy, and a semi-infinite medium don't necessarily apply to myocardium, so we will report the shear velocities c_T directly, and use Shear Wave Velocimetry as its own measurement.[1]

Acoustic Radiation Force (ARF) provides a convenient solution for using a single transducer to excite a shear wave and track its propagation. In the focal region of the excitation beam, the body force is tightly focused laterally, and generates transverse waves that propagate away from the excitation beam (Palmeri et al., 2005). Because the wave displacements are orthogonal to the propagation direction, they are axial displacements relative to the transducer face, and can be tracked with high spatial resolution. Provided that enough stress

[1]While myocardial displacement propagation has often been assumed to be a shear wave (Bouchard et al., 2009a; Couade et al., 2011; Pernot et al., 2011), a number of groups have suggested that an antisymmetric Lamb wave model is more appropriate considering the relatively thin myocardial thickness (Kanai, 2005; Nenadic et al., 2011; Pislaru et al., 2009; Chen et al., 2009). The Lamb wave model includes dispersive effects from the boundary conditions and separates the elastic and viscous components of μ, but the purpose of this paper is to demonstrate the feasibility of using ICE to generate and track transverse waves, and will compare its results to those previously reported using a shear wave model with similar bandwidth (50–350 Hz).

is applied to shear the tissue and create a transverse wave in the field of view, a velocity estimate can be made, independent of amplitude. This provides an advantage over on-axis response methods, like those shown by Hsu et al. (2007a), where the target tissue would move around under the axial region of excitation if not mechanically coupled to the transducer.

Materials and Methods

Experimental Setup

All data presented here were acquired with Siemens AcuNav 10-French ICE catheters, running on a Siemens S2000 scanner. The AcuNav is an FDA-approved, 64-element, 7.25 MHz linear phased array ultrasound transducer, with a 7 mm aperture in azimuth. The small array size is necessary for intracardiac application.

We developed custom pulse sequences to record *in vivo* IQ ultrasound and matched ECG data from six healthy porcine subjects in compliance with protocols from Duke University's Institutional Animal Care and Use Committee (IACUC). The AcuNav was inserted through the jugular vein, and fed through the right atrium into the right ventricle (Fig. 1). Imaging planes were selected for minimal elevational motion and to keep the target tissue as much as possible within a single axial region of excitation (ROE) throughout the cardiac cycle. Motion confounds low-displacement velocity estimates, so with the current setup, targets beyond 20 mm were not considered. The data presented here are taken from long-axis views of the apical interventricular septum (IVS).

Interleaved Tracking

Due to system limitations, the entire lateral field of view can not be imaged simultaneously. Parallel beamforming and dynamic receive focusing only allow up to four A-lines to be recorded from a single transmit event. The parallel receive beams are centered around the focused transmit to maximize SNR while obtaining four separate A-lines in this experiment. 35 groups of four evenly spaced beams span the full 90° field of view, with 2.5° spacing between transmit locations. To image the full propagation of the wave, the superposition of repeated shear wave responses measured at different azimuthal beam groups is used.

Superimposing the responses over the entire 90° field of view would reduce uncertainty in the estimate of shear wave velocity, but it would take an impractically long time to record, as superimposing 35 consecutive responses would undoubtedly span multiple cardiac phases. Because of cardiac motion, minimizing the number of repeated interrogations used to generate a shear wave velocity estimate is essential to achieving quality, high-frame rate data. Fortunately, not all azimuthal angles contribute equally-useful information to the velocity estimate. Geometric spreading causes shear wave amplitudes to fall quickly as they propagate away from the excitation, so wide angles are unlikely so see ARF-induced waves above the physiological motion noise floor. Additionally, within the lateral excitation beamwidth, the observed dynamics are more in response to direct excitation than to the characteristic propagation of the shear wave. The region of interest used in this work is covered by four transmit locations (16 receive locations). These locations are the four closest to the excitation (the center azimuthal line), not including the center transmit or the first transmit to its right. These lines span azimuthally 5° to 14°, which at 15 mm corresponds to a lateral span of 2 mm - 5 mm in the scan-converted data (Fig. 2).

To reduce the number of necessary interrogations even further, we developed sequences that modulate the steering angle of the tracking beams between two azimuthal locations as the wave propagates in response to each excitation. The increased lateral field of view per excitation comes at the expense of the temporal sampling for each imaged line. Using the

maximum frame rate achievable on our scanner with four parallel receive beams, we obtain for each excitation eight 4.56 kHz axial displacement estimates, recorded from 1 ms before excitation through 6 ms post-excitation to allow for interpolated motion estimation. Tracking lines 1–4 and 9–12 are recorded with the first excitation, and lines 5–8 and 13–16 are recorded with the second excitation. This 2-excitation imaging sequence is repeated 160 times at 40 Hz to capture four seconds of shear velocity data throughout multiple cardiac cycles.

Pulse Parameters

For both ARF excitations and tracking beams, 6.15 MHz pulses were used, with available foci between 10 and 20 mm, typically 15 mm. The impulsive excitation was generated with a 400-cycle (65 μs) pulse on the center line of the field of view to maximize acoustic output. The frequency was selected to fall within the bandwidth to the transducer, but below the center frequency to reduce attenuation effects. The shear waves generated by this excitation have frequency content between 50 and 300 Hz. Previous measurements and FEM modeling indicate that for simlilar pulse sequences (15 mm focus and 6 MHz center frequency), Mechanical Index (MI) is under 1.63 and tissue heating is low, 1.01°C over four seconds with 40 2-excitation acquisitions per second.

Shear Wave Speed Estimation

Figure 3 shows a flowchart of the signal processing chain used to obtain shear wave velocity estimates from the recorded IQ echo data. As described in detail by Hsu et al. (2007a), a phase-shift based displacement estimator (Kasai et al., 1985) is used to calculate the ARF induced displacements, using a 1.5- λ kernel. Once the displacements have been calculated, a quadratic motion filter is used to remove the bulk axial motion of the tissue from the ARF-induced displacements (Giannantonio et al., 2011). At each pixel, the displacement estimates from before the excitation and those greater than 3 ms after the excitation are fit to a quadratic function as an estimate of physiological motion. The motion is interpolated over the 3 ms after the excitation and subtracted from the data. The displacement estimates are then interpolated temporally to fill in the missing time steps due to the steering angle modulation and scan-converted into Cartesian coordinates with 0.1 mm x 0.1 mm pixel spacing.

Each of the 401 axial slices of the scan-converted image is considered independently for velocity estimation. Each axial slice is filtered with a second order temporal Butterworth bandpass filter with cutoff frequencies of 50 and 350 Hz to reduce noise outside of the expected bandwidth of the propagating wave. To compensate for reactive transducer kick-back, spatio-temporal locations in each slice that would correspond to shear wave speeds below 0.5 m/s (late times and near the excitation) or above 8 m/s (early times and far from the excitation) are assumed to be due to kick-back. A single kick-back profile is estimated from the average displacements and subtracted from the slice, leaving only the propagating shear wave. To estimate the wave velocity, a version of the algorithm described by Palmeri et al. (2008) is used. The time-to-peak-displacement is then calculated for each lateral pixel. The time-to-peak data are then fit by linear regression, automatically removing outliers from motion artifact that cause the residual of the linear fit to fall below 0.5. The velocity is calculated at each depth, forming an A-line of velocity estimates, which, when repeated over the 160 acquisitions, forms a shear velocity M-mode image.

Region of Interest Tracking

Because the myocardium is moving relative to the transducer, anatomical locations will appear at different locations within the imaging plane at each shear wave acquisition. Within the M-mode of velocity estimates, the depths that are tissue and those that are blood will

vary from frame to frame. Tracking the tissue borders improves visualization of the time-varying characteristics of the target tissue, and permits observation of axial stiffness variation.

To alleviate the need to manually segment every frame, nonrigid elastic registration, as detailed by Kybic and Unser (2003) was utilized to compute the motion between frames. Nonrigid elastic registration has been previously applied to ultrasound images to assess motion and strain (Ledesma-Carbayo et al., 2005; Elen et al., 2008; Myronenko et al., 2007). A multidimensional B-spline deformation model is used to estimate the warping function that describes the motion between each frame. This algorithm finds the deformation function $g(\mathbf{x})$ that optimally relates the test image f_t to the reference image f_r. To constrain the amount of warping of the image, the cost function used has terms for the sum-of-squared-difference (SSD) between the unwarped image and the target, as well as adjustable weighting functions for the gradient and curl of the computed displacement field:

$$E = w_{im} E_{im} + w_{div} E_{div} + w_{rot} E_{rot} \quad (2)$$

For these experiments, a knot spacing of 7 mm laterally and 5 mm axially was used. The weightings for w_{im}, w_{div}, and w_{rot} were 1, 2, and 1, respectively. For each sequence of data, a matched B-mode image was acquired immediately prior to each shear wave acquisition. These B-mode images were unwarped using the freely-available ImageJ (Abramoff et al., 2004) plugin UnwarpJ(Sorzano et al., 2005), and the transformation parameters describing each $g_j(x)$ saved. The proximal and distal tissue borders for the IVS (x_{p1}, x_{d1}) were manually marked in the first frame of each dataset. The computed transformations $g_j(x)$ were applied to the marked points in the reference image to compute their warped locations in the subsequent frames (x_{pj} and x_{dj}). This automatically outlined the borders of the myocardium for most frames, with manual segmentation being used for those frames with obvious registration errors. While this allows the IVS's axial-lateral location to be tracked in each frame and accounted for, the lateral ROI is necessarily limited by the region of excitation and the location of the tracking beams in this implementation. Additionally, although the septum is tracked through each frame, the axial region of excitation limits the depths over which transverse waves can expect to be generated. Thus the final ROI to be considered is the intersection of the axial tissue region (typically 1–2 cm thick) as determined by the unwarping, and the region of excitation. The dynamic ROI calculated by unwarping is then used to window the shear wave velocity data, which have been independently calculated at every axial location.

Multi-beat Synthesis

To compare data acquired across multiple heartbeats, a technique called multi-beat synthesis (Hsu et al., 2007b) was used to register estimates from many frames onto a single heartbeat. The time of each ARF excitation is acquired with the ECG data. Each shear wave velocity estimate is thus assigned a fractional delay from the QRS complex in terms of the R-R interval. All of the shear wave velocity estimates can then considered relative to a single, normalized heartbeat, grouped by their cardiac phase. 64 evenly spaced delays were used to group the velocity estimates over the cardiac cycle.

Results

Figures 4–9 follow a single set of 160 acquisitions over four seconds from motion tracking through multibeat synthesis to demonstrate the post processing and generation of quantitative results. Figure 4 shows the center line of the B-mode image acquired with each acquisition as an M-mode for a single imaging sequence viewing the IVS. Highlighted on

the image is the proximal septal boundary, as calculated in each frame by automatic registration. The motion of the septum is at times large, but very repeatable, and parts of the tissue remain in the expected region of excitation (5–10 mm) throughout the cardiac cycle. Figure 5 shows the relative amplitude of scan-converted ARF displacements (averaged over the first 3 mm and 1 ms because the on-axis data are not recorded) through depth and across the 160 acquisitions for the same sequence shown in figure 4. Qualitatively, there is clear variation in the displacement magnitude, as seen previously in M-Mode ARFI experiments (Hsu et al., 2007a), but the axial motion obfuscates a quantitative assessment.

Figure 6 shows axial slices of the spatio-temporal volumes across the cardiac cycle, taken at the middle of the septum from the same pig, and post kickback filter. The slices are consecutive, left-to-right, top to bottom, with each row covering a seperate heart beat. Systole and diastole are marked on the ECG below. Though noisy, the amplitude of the transverse wave varies as indicated in figure 5, and the angle of the propagating wave (which corresponds to the velocity) varies with the cardiac cycle. The response across multiple beats is very repeatable. Systolic shear wave amplitudes tend to start around 5 μm near the excitation, and fall to 2 μm over 3 mm of propagation. Diastolic estimates, on the other hand, initially have 10–12 μm of amplitude, falling to 4–6 μm as they propagate. Figure 7 shows the M-Mode of shear wave velocity estimates through depth and across the 160 acquisitions, along with the axial median shear wave velocity. The highlighted region of interest is the intersection of the axial ROE and the tracked tissue boundaries. Despite the low quality of many of the slices in figure 6, clear, repeatable variation is seen through the cardiac cycle. The individual estimates show variability, but the overall trend of stiffening and relaxation between 0.9–1.1 m/s and 3.5–5 m/s is clear. Diastolic estimates are especially smooth. Some axial variation is also seen, with the deeper systolic estimates appearing slightly elevated, but the temporal trends of stiffening and relaxation with the cardiac cycle dominate.

Figure 8 shows the distribution of individual velocity estimates from figure 7 in systole and diastole, as indicated by the cyan- and yellow-shaded regions on the ECG in figure 7. The mean values indicate a lower velocity ratio than the median values. Figure 9 shows the multibeat-synthesized data from figure 7. The variation through the cardiac cycle is clear and smoothly varying. A small amount of axial variation is present, but the predominant trend is temporal, with relatively stable velocities during diastole and systole, and a sharp rise in velocity at the onset of systole and a slightly more gradual relaxation at the beginning of diastole. The standard deviations are higher in systole than in diastole, and approximately proportional to the shear wave velocity. Figure 10 shows the shear velocity M-Modes and median velocities for the six animals. Heart rates and motion vary among the animals greatly. The quality of the images from the animals with elevated heart rates (3, 5) appears much worse than those with lower heart rates (1, 2, 4, 6). Table 1 shows the compiled systolic and diastolic shear wave statistics like those shown in figure 8 for each of the six pigs. The means, medians, and standard deviations of all of the velocity estimates are reported from the 160-acquisition sequences like those shown in figure 10. The ratios of means and medians are also shown. The mean diastolic velocities range from 1.42 to 2.68 m/s, and the mean systolic velocites range between 3.06 and 5.12 m/s. The median velocities, on the other hand, range between 0.89 and 2.2 m/s in diastole and 2.60 and 5.14 m/s in systole. The standard deviations of the systolic velocities ranged between 1.49 and 1.92 m/s and the standard deviations of the diastolic velocities ranged between 0.95 m/s and 1.76 m/s. The systolic-diastolic ratio of means range between 1.77 and 3.02 and the ratio of the medians range between 2.1 and 3.66.

Comparison to Previous Studies

Our results are compared to those previously reported using open chest ARF-driven velocimetry technique, as well as to Kolipaka *et al*'s human MRE experiment(Kolipaka et al., 2010) and Kanai's Aortic Valve Closure (AVC) data(Kanai, 2005) in closed-chest human septum in Table 2 . Tabulated are the different experimental set-ups used to measure myocardial elasticity, as well as the estimated shear modulus in systole and diastole, and the ratios of systolic to diastolic shear modulus. The measured elasticities of this experiment mostly fall within the range of values reported in open-chest studies, although the diastolic estimates from pigs 2, 3, and 6, and the systolic estimate from pig 3 appear higher than previously seen. Compared to the MRE experiment, our diastolic velocities are lower and the systolic velocities distributed around the MRE result. Kanai's AVC data indicate systolic stiffness as high or higher than we measured. Overall, none of the data reported here for diastole or systole fall outside of the range of previously reported myocardial stiffnesses or ratios. Figure 11 shows the results of this experiment and the results of the other myocardial elasticity experiments from Table 2 as shear wave velocities rather than shear moduli for visual comparison. The results from this experiment are listed as "1" through "6" and are shown to be similar to those previously demonstrated.

Discussion

These results clearly indicate the feasibility of using shear wave velocimetry to image myocardial stiffness and contractility throughout the cardiac cycle with an ICE catheter probe. Despite the hardware limitations of the current platform, we were able to use creative beam sequencing to image both diastolic and systolic shear waves with the superposition of only two responses, providing rapid temporal sampling that captures the dynamic stiffening and relaxation of the septum. With the catheter placed near the apex of the RV, long axis views of the IVS were readily attained with sufficient thickness, repeatable motion, and high contractility. Views of the RVFW and of the free wall and septum in the RA were also available, but are not presented here because the RVFW in our young pigs was rather thin (less than 2 mm) and the RA has much lower contractile properties. These regions are likely candidates for further study and the regionally-varying dynamic elastic properties of the heart may provide additional information, but for the purposes of demonstrating the feasibility of using ICE to measure cardiac shear wave velocities *in vivo*, the IVS yields compelling data.

With motion filtering, the ARF-induced displacements were mostly separated from the bulk tissue motion and imaged, although in many cases the tissue motion and displacement estimation jitter were too great, resulting in motion artifact as seen in some of the frames of figure 6. Because of this variability in individual wave propagation estimates, putting the data synthesis at the end of our signal processing chain provides a larger number of observations to use, which in turn gives more confidence in our quantitative results. Using separate axial estimates and multi-beat synthesis, we are able to use over 1000 individual estimates for each phase as reported in table 2. Using median values reduces the effect of outliers, which would otherwise affect mean values especially if bad time-to-peak displacement estimates are close together, causing the estimated velocity to trend towards infinity. Obtaining many noisy velocity estimates and then combining them together appears to work better than averaging the displacements axially and finding a single estimate as is normally done, at least in the case of small displacements and high motion. A single depth's displacement profile corrupted by motion could throw off the entire estimate of time-to-peak displacement and thus shear wave velocity for the kernel, but processing each depth independently avoids this because individually bad estimates can be filtered amidst otherwise good estimates.

In Vivo Results

The diastolic and systolic velocities across all animals varied among animals, but the ratios were more consistent. The first pig had the highest ratio, but was also the oldest, with the thickest septum, which could be the reason for the increased contractility. The second and third pigs in figure 10 had elevated median diastolic velocities, although the minimum velocities appear visually similar to the first pig in figure 10. The shortened length of diastole due to the elevated heart rates of these animals could be contributing to this, although in the second pig, the 4th and 5th beats have very clean and consistent data in diastole with visually elevated velocities. The third pig has a higher heart rate than the second, and the distal part of its septum appears to behave similarly to the first pig, although the proximal tissue appears very noisy. The source of spatial variation could be due to the field of view. The third pig was imaged with a focal depth of 10 mm, and the proximal side of the ROE is at 5 mm, so the lateral extent of the field of view at the shallow depths is only 1–2.5 mm. For shallow imaging, a different set of steering angles for wave tracking may yield superior results. The fourth pig had a very thin septum (2.5 mm in systole and 5 mm in diastole) with high motion, which may indicate that a different model (i.e. Lamb wave) would be more appropriate, but the velocity trends are consistent with the others. Following the tissue as it moves axially, the velocities consistently rise in systole and fall in diastole. This animal would be difficult to analyze with M-Mode ARFI due to the motion, but appears usable with SWV. The fifth pig initially looks especially bad, but its heart rate was above 150 BPM, and repeatable velocity peaks are in fact seen which correspond to systole. When calculating the ratios, however, the values for diastole and systole appear normal, although systole is the low end, likely due to the very short systolic duration. The sixth pig has respiration motion, as well as axial variation in shear wave speeds, but otherwise exhibits the same characteristic stiffening and relaxation. Only in pigs 4 and 6 is the proximal edge of the septum within the ROI, so similar spatial trends may be present in the other animals. This could be due to the intrinsic anisotropy of the septum due to fiber orientation, or to differences in RV and LV contractility. The distal portion of pig 6's septum look more like pigs 1–3, but the spatial variation causes the median systolic value to be lower. Accounting for the variability among animals, and exploring the regional variations in contractility will be the topic of future work. Nonetheless, in all of the animals, we can see clear temporally-varying shear wave speeds with each heartbeat.

Comparison to Previous Studies

All of measured velocities in this experiment are within the ranges reported in the literature for myocardium in systole and diastole. There are, however, substantial differences within the values reported in the literature. A more elaborate experiment may need to be devised to compare the ultrasonically measured results to a gold standard like mechanical testing, although excised tissue degrades quickly and obtaining the exact interrogated piece of tissue in the same condition with the same fiber orientation would be difficult, as would applying the same pressures experienced *in vivo*. What would possibly be the closed-chest gold standard for comparison, MRE, is limited by being a global metric. Kolipaka *et al.* modeled the LV as a homogeneous shell; contractility variation, whether spatially or in timing, could be the source of the much lower reported ratio. Using the previously reported ultrasound data as a reference, the ranges of values measured here using ICE appear at least comparable. The differences between our results and those previously reported, and within those previously reported, could come from a number of sources. Different animal models and tissue targets were used which would certainly introduce variation, but even our data, which are all from pigs, show substantial animal-to-animal variability in the long-axis IVS. Anisotropy affected the shear speeds but not the ratios in Couade *et al.*'s work, and the fibrous nature of myocardium warrants further exploration of this where possible. Pernot *et al.* show a linear dependence on pre-load for systolic moduli between 80 and 160 mmHg,

which could explain some of the systolic variability that we have seen. Dispersive methods like that shown by Pislaru *et al.* use the phase velocities to find frequency dependent velocities, and the characteristic excitation varies between the experiments, so the spectral content of the propagating wave is yet another source of variation. Within the same experimental set-up, however, the excitation is constant, and the variation is likely due to actual variations in pressure or regional tissue properties.

Limitations and Future Work

The biggest limitations of this experiment were system capabilities. The scanners that currently support running customized ARF sequences on the AcuNav are capable of beamforming only four azimuthal lines per transmit. Newer systems can beamform more simultaneous lines, or even store individual channel data. Adapting these systems to work with the AcuNav would permit use of a defocused transmit for the tracking pulse and imaging the entire field of view simultaneously. Wide field-of-view tracking would improve velocity estimates by reducing the number of excitations needed from two to one, allowing simultaneous tracking of waves to the left and right of the excitation, and providing additional azimuthal locations for motion and kick-back filtering. With finer temporal sampling, we would be able to capture the dynamics of contraction and relaxation better, especially for cases of elevated heart rates. Future work will also include pressure measurements to normalize the effect of pre-load on systolic measurements (Pernot et al., 2011).

The spatially-varying properties may be the most interesting subject to explore, and a longer axial ROE, obtained with multiple excitations, would improve our ability to image these variations. Because the AcuNav is an FDA approved device, and the MI and thermal measurements and simulations indicate safety, clinical translation should be possible. Clinical work will also need to be done to determine the quantitative relationship between tissue health and observed transverse wave propagation, with respect to both the tissue model and the nature of the excitation. This study was performed on the IVS, but LV contractility has typically been the parameter of interest. Further work needs to be done to relate properties measured in the IVS to those measured in the LVFW for indicating LV function. Extending this work to image the LVFW directly is also an area of future study, and we have identified two potential solutions. The first would be to insert the ICE transducer into the LV, either retrograde across the aortic valve or across the atrial septum and through the LA, although both of these entry paths carry additional risks. The second would be to use a larger or lower frequency ICE transducer to generate focused radiation force in the LVFW from the catheter in the RV. The second solution is likely more favorable from a safety standpoint, but may require a specialized transducer to generate sufficient radiation force at depth.

Conclusions

We have demonstrated the viability of using intracardiac echocardiography linear phased arrays to perform ARF-based velocimetry in myocardium though the cardiac cycle. We have shown cyclically varying shear wave speeds in the interventricular septum across six healthy animals, with systolic to diastolic shear modulus stiffness ratios between 4.4 and 13.4. Customized beam sequences make this measurement in sets of acquisitions at up to 40 frames per second. Operating within FDA limits, the AcuNav is well suited for clinical studies to explore the relationship between ARF-induced shear wave speeds and cardiac function. With appropriate considerations of the dynamic intracardiac environment, ARF shear wave velocimetry from an ICE catheter provides a minimally invasive way to quantify myocardial elasticity and contractility in the beating heart.

Acknowledgments

References

Abramoff M, Magalhaes P, Ram S. Image processing with imagej. Biophotonics International. 2004; 117:36–42.

Bleeker G, Steendijk P, Holman E, Yu CM, Breithardt O, Kaandorp T, Schalij M, van der Wall E, Nihoyannopoulos P, Bax J. Assessing right ventricular function: the role of echocardiography and complementary technologies. Heart. 2006; 92:19–26.

Bouchard R, Dahl J, Hsu S, Palmeri M, Trahey G. Image quality, tissue heating, and frame rate trade-offs in acoustic radiation force impulse imaging. IEEE Trans UFFC. 2009a; 561:63–76.

Bouchard R, Hsu S, Palmeri M, Rouze N, Nightingale K, Trahey G. Acoustic radiation force-driven assessment of myocardial elasticity using the displacement ratio rate (drr) method. Ultrasound Med Biol. 2011; 377:1087–1100. [PubMed: 21645966]

Bouchard R, Hsu S, Wolf P, Trahey G. In vivo cardiac, acoustic-radiation-force-driven, shear wave velocimetry. Ultrasound Imaging. 2009b; 313:201–213.

Chen S, Urban M, Pislaru C, Kinnick R, Zheng Y, Yao A, Greenleaf J. Shearwave dispersion ultrasound vibrometry (sduv) for measuring tissue elasticity and viscosity. IEEE Trans Ultrason. 2009; 561:55–62.

Chu E, Fitzpatrick A, Chin M, Sudhir K, Yock P, Lesh M. Radiofrequency catheter ablation guided by intracardiac echocardiography. Circulation. 1994; 89:1301–1305. [PubMed: 8124819]

Couade M, Pernot M, Messas E, Bel A, Ba M, Hagege A, Fink M, Tanter M. In vivo quantitative mapping of myocardial stiffening and transmural anisotropy during the cardiac cycle. IEEE Trans Med Imag. 2011; 302:295–305.

D'Hooge J, Heimdal A, Jamal F, Kukulski T, Bijnens B, Rademarers F, Hatle L, Suetens P, Sutherland G. Regional strain and strain rate measurements by cardiac ultrasound: Principles, implementation and limitations. Eur J Echocardiogr. 2000; 11:154. [PubMed: 11916589]

Elen A, Loeckx D, Gao H, Claus P, Suetens P, Maes F, D'hooge J. Three-dimensional cardiac strain estimation using spatio-temporal elastic registration of ultrasound images: A feasibility study. IEEE Trans Med Imag. 2008; 2711:1580–1591.

Eyerly S, Hsu S, Agashe S, Trahey G, Li Y, Wolf P. An in vitro assessment of acoustic radiation force impulse imaging for visualizing cardiac radiofrequency ablation lesions. Journal of Cardiovascular Electrophysiology. 2010; 215:557–563. [PubMed: 20021518]

Giannantonio D, Dumont D, Trahey G, Byram B. Comparison of physiological motion filters for in vivo cardiac arfi. Ultrasonic Imaging. 2011; 332:89–108. [PubMed: 21710825]

Haddad F, Hunt S, Rosenthal D, Murphy D. Right ventricular function in cardiovascular disease, part i: Anatomy, physiology, aging and functional assessment of the right ventricle. Circulation. 2008; 117:1436–1448. [PubMed: 18347220]

Hsu S, Bouchard R, Dumont D, Wolf P, Trahey G. In vivo assessment of myocardial stiffness with acoustic radiation force impulse imaging. Ultrasound Med Biol. 2007a; 3311:1706–1719. [PubMed: 17698282]

Hsu S, Fahey B, Dumont D, Wolf P, Trahey G. Challenges and implementation of radiation-force imaging with an intracardiac ultrasound transducer. IEEE Trans UFFC. 2007b; 545:996–1009.

Kanai H. Propagation of spontaneously actuated pulsive vibration in human heart wall and in vivo vescoelasticity estimation. IEEE Trans UFFC. 2005; 5211:1931–1942.

Kasai C, Namekawa K, Koyano A, Omoto R. Real-time two-dimensional blood flow imaging using autocorrelation technique. IEEE Trans Sonics Ultrason. 1985; 32:458–463.

Kolipaka A, Araoz PA, McGee KP, Manduca A, Ehman RL. Magnetic resonance elastography as a method for the assessment of effective myocardial stiffness throughout the cardiac cycle. Magnetic Resonance in Medicine. 2010; 643:862–870. [PubMed: 20578052]

Kybic J, Unser M. Fast parametric elastic image registration. IEEE Trans Image Proc. 2003; 1211:1427–1442.

Langeland S, D'hooge J, Wouters P, Leather H, Claus P, Bijnens B, Sutherland G. Experimental validation of a new ultrasound method for the simultaneous assessment of radial and longitudinal myocardial deformation independent of insonation angle. Circulation. 2005; 112:2157–2162. [PubMed: 16203928]

Ledesma-Carbayo M, Kybic J, Desco M, Santos A, Sühling M, Hunziker P, Unser M. Spatio-temporal nonrigid registration for ultrasound cardiac motion. IEEE Trans Med Imag. 2005; 249:1113–1126.

Mebazaa A, Karpati P, Renaud E, Algotsson L. Acute right ventricular failure – from pathophysiology to new treatments. Intensive Care Med. 2004; 30:185–196. [PubMed: 14618229]

Mullen M, Dias B, Walker F, Siu S, Benson L, McLaughlin P. Intracardiac echocardiography guided device closure of atrial septal defects. J Am Coll Cardiol. 2003; 412:285–292. [PubMed: 12535824]

Myronenko A, Song X, Sahn D. Lv motion tracking from 3d echocardiography using textural and structural information. MICCAI. 2007; 4792:428–435. [PubMed: 18044597]

Nenadic I, Urban M, Mitchell S, Greenleaf J. Lamb wave dispersions ultrasound vibrometry (lduv) method for quantifying mechanical properties of viscoelastic solids. Phys Med Biol. 2011; 56:2245–2264. [PubMed: 21403186]

Palmeri M, Sharma A, Bouchard R, Nightingale R, Nightingale K. A finite-element method model of soft tissue response to impulsive acoustic radiation force. IEEE Trans UFFC. 2005; 5210:1699–1712.

Palmeri M, Wang M, Dahl J, Frinkley K, Nightingale K. Quantifying hepatic shear modulus in vivo using acoustic radiation force. Ultrasound Med Biol. 2008; 34:546–558. [PubMed: 18222031]

Pernot M, Couade M, Mateo P, Crozatier B, Fischmeister R, Tanter M. Real-time assessment of myocardial contractility using shear wave imaging. J American College of Cardiology. 2011; 51:65–72.

Pislaru C, Urban M, Nenadic I, Greenleaf J. Shearwave dispersion ultrasound vibrometry applied to in vivo myocardium. EMBC. 2009; 2009:2891–2894.

Sarvazyan A, Rudenko O, Swanson S, Fowlkes J, Emelianov S. Shear wave elasticity imaging; a new ultrasonic technology of medical diagnostics. Ultrasound Med Biol. 1998; 249:1419–1436. [PubMed: 10385964]

Serri K, Reant P, Lafitte M, Berhouet M, Bouffos VL, Roudaut R, Lafitte S. Global and regional myocardial function quantification by two-dimensional strain: Application in hypertrophic cardiomyopathy. J American College of Cardiography. 2006; 621:1175–1181.

Sorzano C, Thévenaz P, Unser M. Elastic registration of biological images using vector-spline regularization. IEEE Trans Biomed Eng. 2005; 424:652–663. URL http://bigwww.epfl.ch/thevenaz/UnwarpJ/. [PubMed: 15825867]

Westermann D, Kasner M, Steendijk P, Spillmann F, Riad A, Weitmann K, Hoffman W, Poller W, Pauschinger M, Schultheiss H, Tschöpe C. Role of left ventricular stiffness in heart failure with normal ejection fraction. Circulation. 2008:117. [PubMed: 20031553]

Wolf P, Eyerly S, Bradway D, Dumont D, Bahnson T, Nightingale K, Trahey G. Near real time evaluation of cardiac radiofrequency ablation lesions with intracardiac echocardiography based acoustic radiation force impulse imaging. Presented at 161st meeting of the Acoust Soc Amer, J Acoust Soc Amer. 2011; 1294:2438–2438.

Zile C, Baicu F, Gaasch W. Diastolic heart failure- abnormalities in active relaxation and passive stiffness of the left ventricle. N Engl J Med. 2004; 350:1953–1959. [PubMed: 15128895]
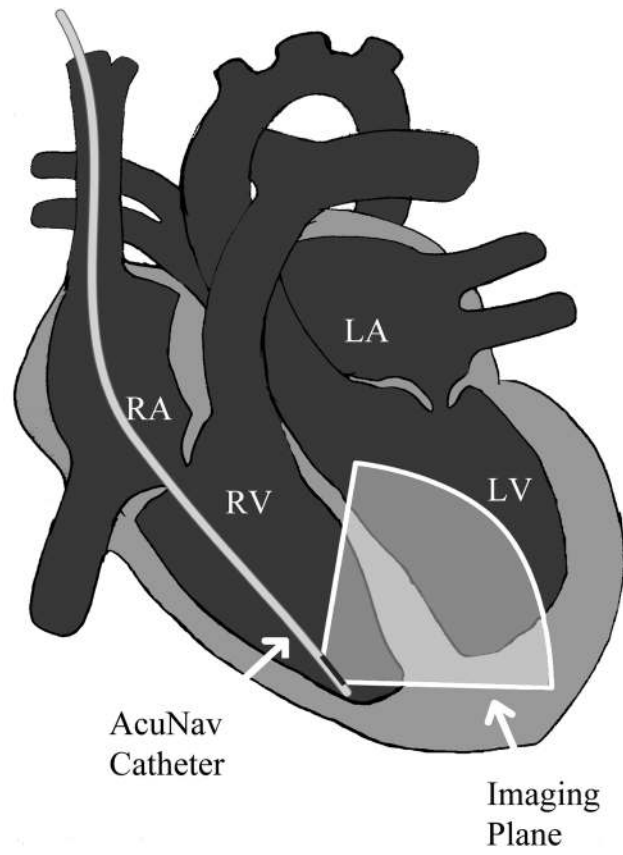
Figure 1.
Ultrasound catheter tip placement. The imaging plane transects the interventricular septum.
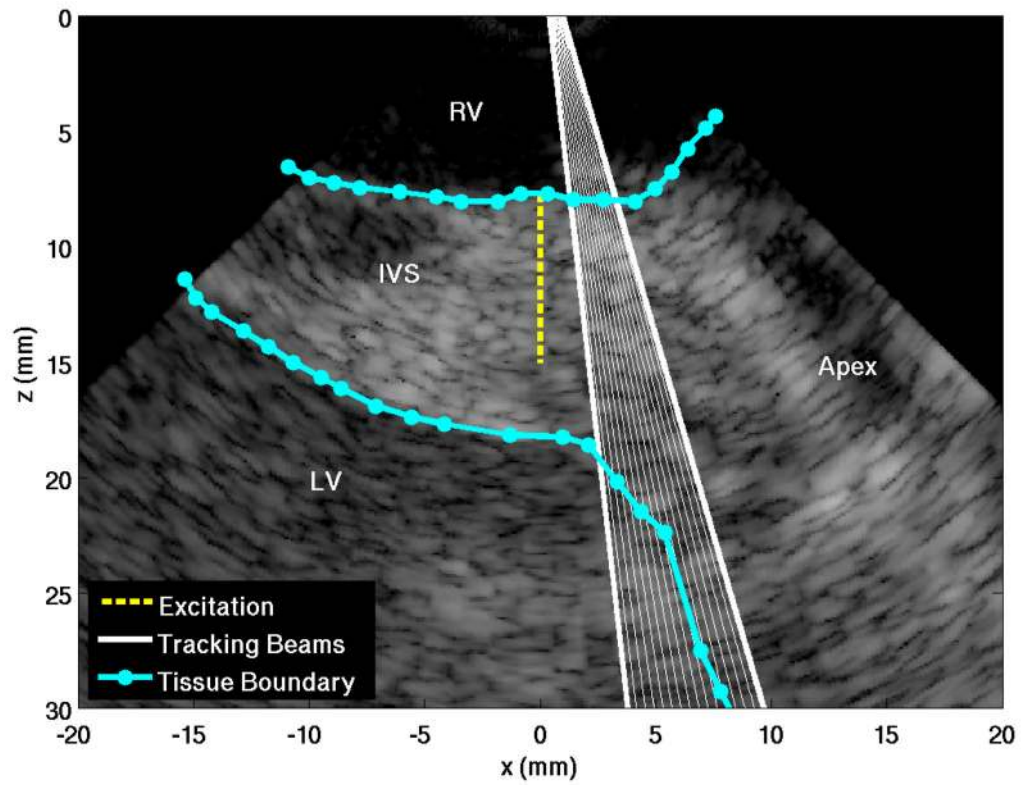
Figure 2.
Shear Wave Imaging field of view. The ARF excitation is along the center of the image, generating displacements about the 15 mm focus, which are tracked propagating towards the apex.
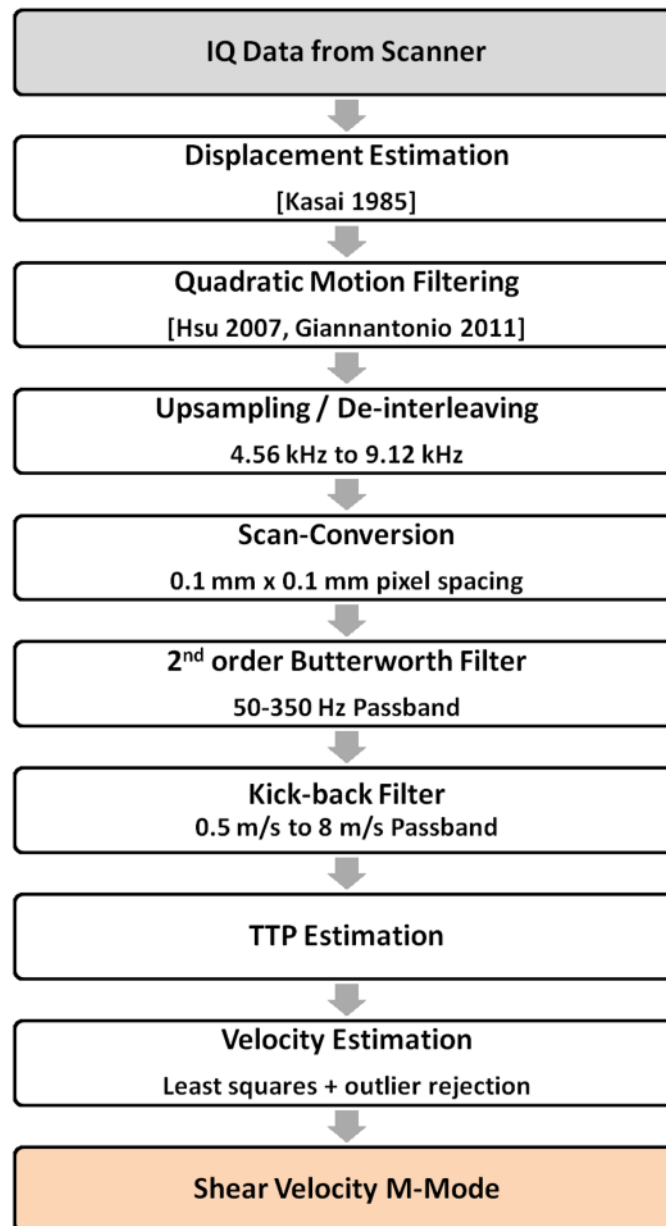
Figure 3.
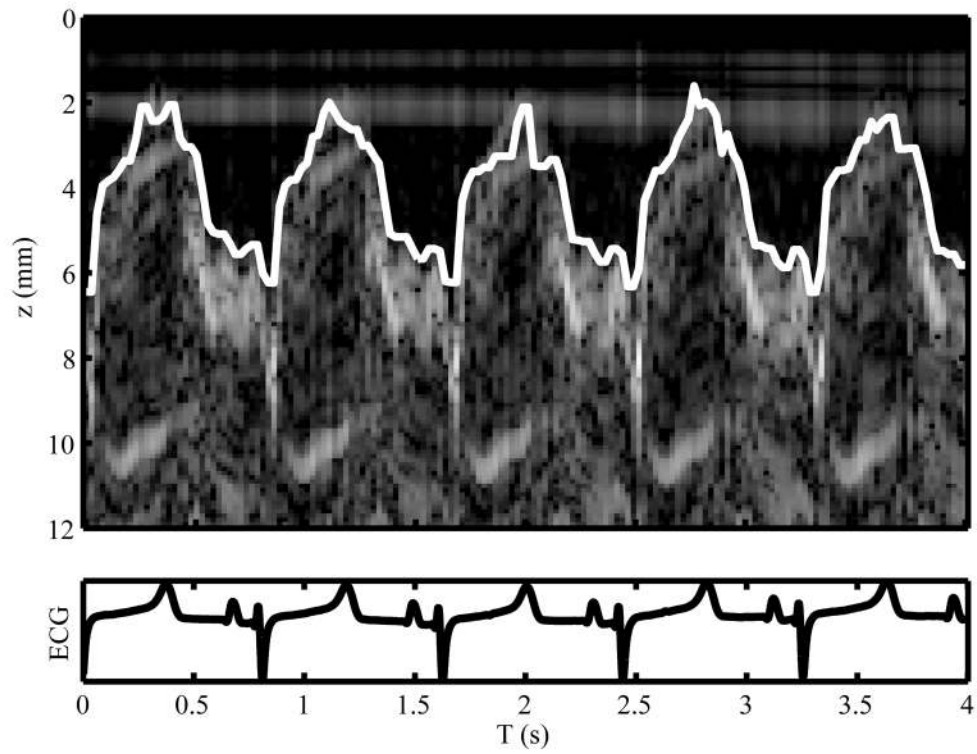Data processing sequence from IQ data to shear wave velocities.

Figure 4.
Axially tracked M-Mode of the IVS. The proximal border of the septum is drawn in white. The motion of the tissue varies repeatably with the cardiac cycle.
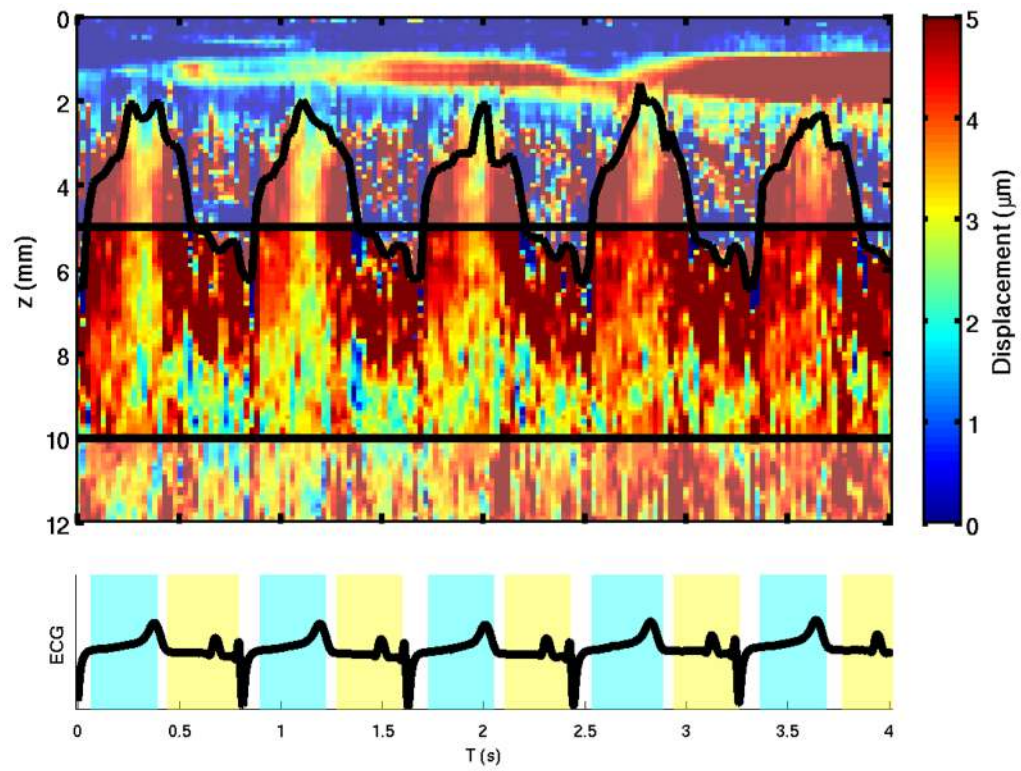
Figure 5.
Transverse wave magnitude in IVS. Black lines indicate the expected region of shear wave generation, between 5 mm 10 mm. The displacement magnitude varies with depth and with the cardiac cycle. Cyclic variation of the displacements is seen with the cardiac cycle, but the axial motion obfuscates estimation of elastic properties.
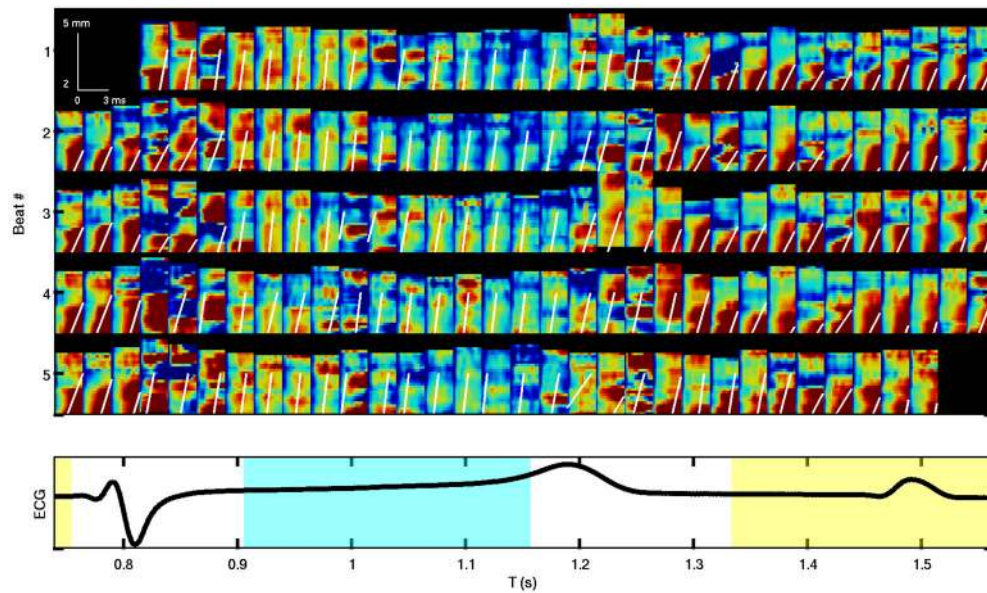
Figure 6.
A selected axial slice of displacement data from each of 160 acquisitions through five heart beats, left to right, top to bottom, selected from the center of the septum. The time-to-peak-displacement fit is superimposed. Blue is no displacement, and red is 8 μm displacement. Systolic slices have steeper slopes (indicating faster propagation) and typically lower amplitudes than diastolic slices. Many of the slices are corrupted by motion. Each image spans 3 ms after the excitation and 2–5 mm laterally.
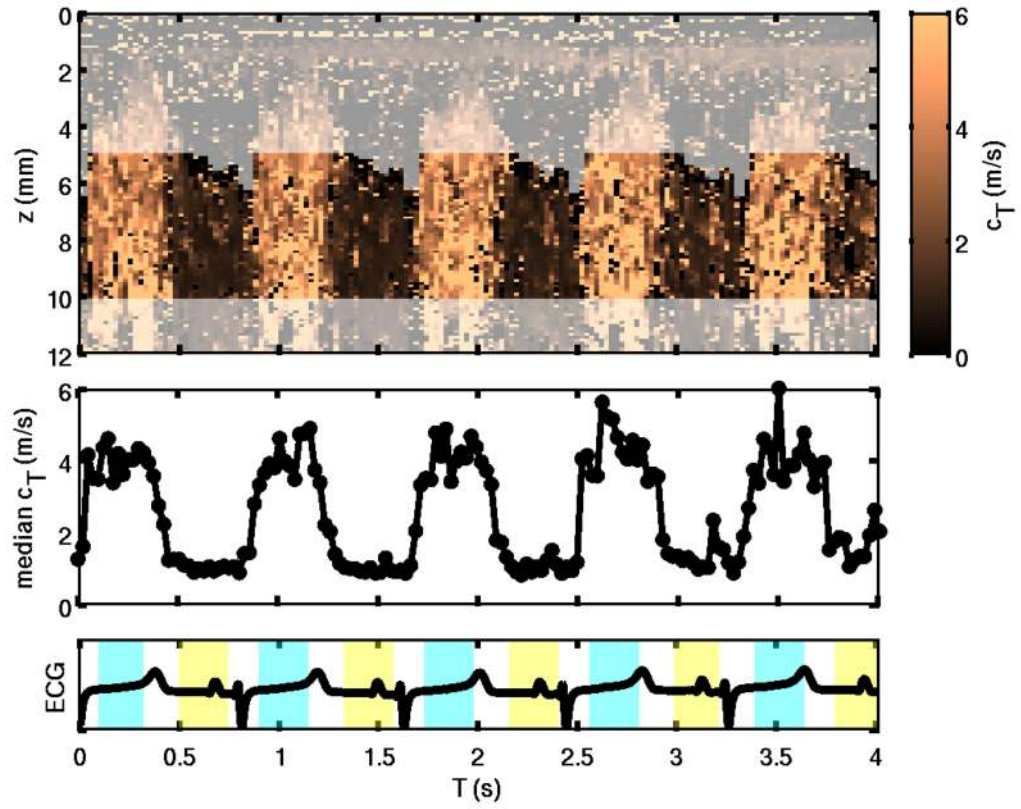
Figure 7.
Shear wave velocities through depth (M-Mode) and axial median shear wave velocities across IVS, through five heartbeats. The highlighted region from 5–10 mm represents the intersection of the axial region of excitation (ROE) and the septal tissue location. The beat-to-beat repeatability of the stiffening and relaxation is very high, with systolic velocities between 3.5 and 5 m/s and diastolic velocities between 0.9 and 1.1 m/s.
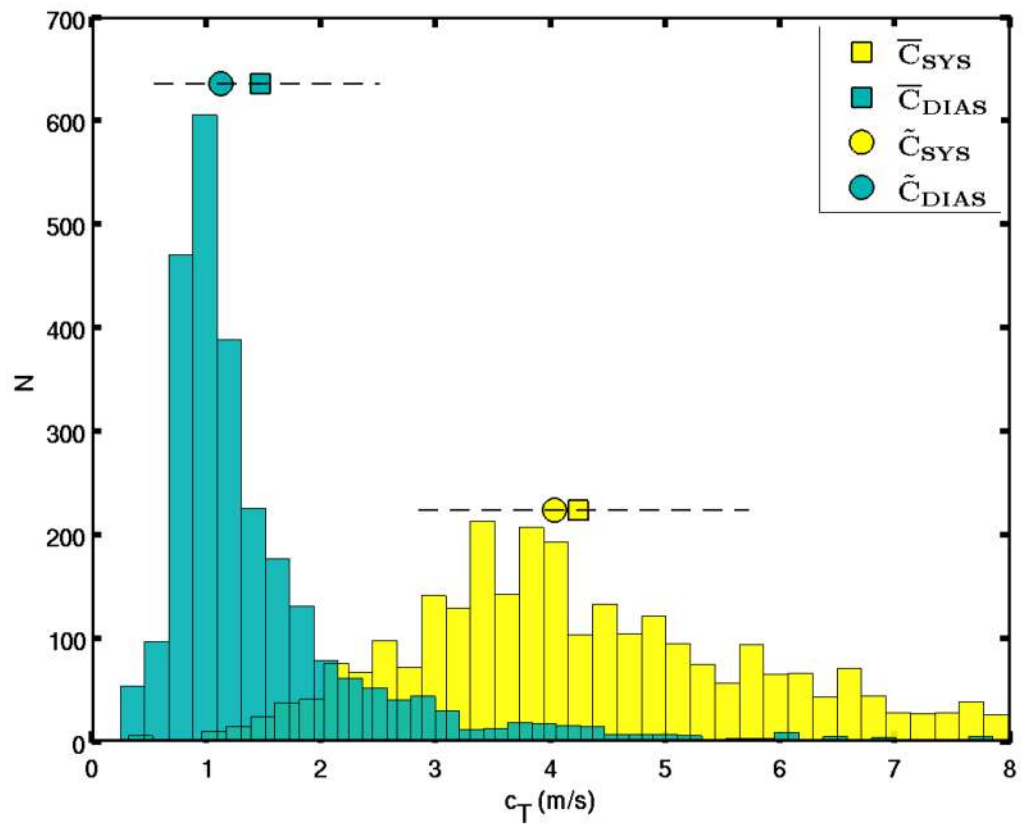
Figure 8.
Distribution of all diastolic and systolic shear wave speed estimates over 160 acquisitions, extracted from Figure 7 according to the cyan and yellow shaded regions of the ECG. The medians and means are marked as squares and circles, respectively. The systolic-diastolic ratio of medians is 3.66 and the ratio of means is 3.02.
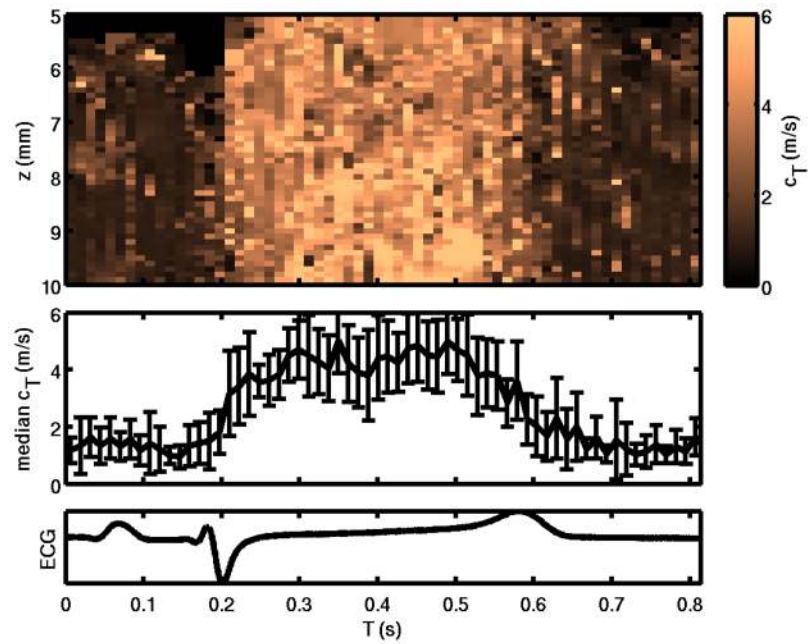
Figure 9.
Multibeat synthesis of the M-Mode SWEI from figure 7 and respective axial median using 5 heartbeats of data. The trends visible in figure 7 remain, with reduced noise. The rise in stiffness immediately following the QRS complex is particulary sharp.
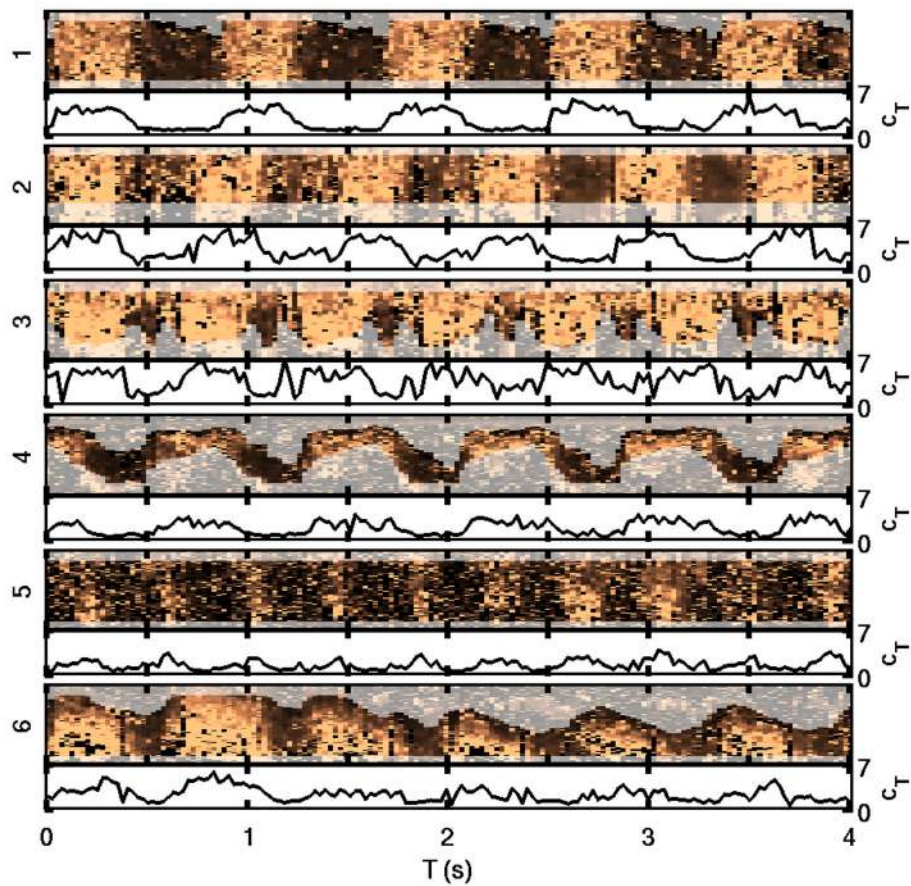
Figure 10.
Shear wave velocity M-Modes and axial median profiles for each of the six Pigs. Regions that fall either outside the tissue or outside of the region of excitation (ROE) are greyed out. Rejected estimates appear as black pixels. The color ranges from 0 m/s (dark brown) to 6 m/s (tan) The quality of the images declines with higher heart rates (pigs 3 and 5). All pigs exhibit cyclic variation of velocities.
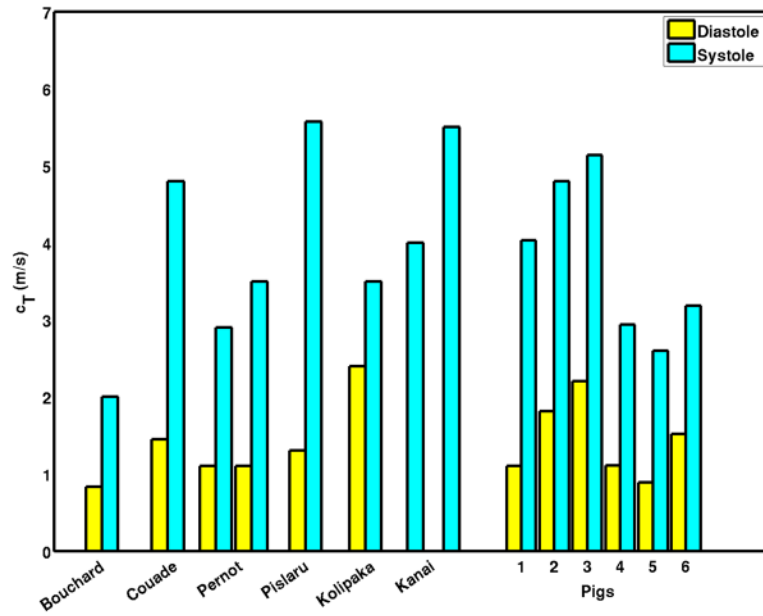
Figure 11.
Comparison of shear wave velocities from this experiment with those previously reported in the literature. The methodology, animal model, and tissue targets vary between experiments, and all data re- ported as shear moduli have been converted to shear wave velocities.

Table 1

Ages, Weights, Heart Rates (HR), Non-invasive Blood Pressure (NBP), and Systolic and diastolic septal shear wave velocity estimates for six healthy pigs.

Pig	#	1	2	3	4	5	6
Age	days	123	72	74	76	81	74
Weight	kg	42.9	32.7	28.1	29.9	23.0	33.3
HR	BPM	73.7	87.7	102.3	77.1	148.0	91.8
NBP	mmHg	89/47	69/28	88/30	89/40	92/32	85/41
$\bar{c}_{sys}$	m/s	4.28	4.87	5.12	3.07	3.06	3.47
$\tilde{c}_{sys}$	m/s	**4.03**	**4.80**	**5.14**	**2.94**	**2.60**	**3.18**
σ_{sys}	m/s	1.49	1.61	1.60	1.71	1.78	1.92
$\bar{c}_{dias}$	m/s	1.42	2.15	2.68	1.50	1.49	1.97
$\tilde{c}_{dias}$	m/s	**1.10**	**1.81**	**2.20**	**1.11**	**0.89**	**1.52**
σ_{dias}	m/s	0.95	1.27	1.76	1.09	1.45	1.29
$\bar{c}_{sys}/\bar{c}_{dias}$		3.02	2.26	1.91	2.05	2.05	1.77
$\tilde{c}_{sys}/\tilde{c}_{dias}$		**3.66**	**2.66**	**2.34**	**2.64**	**2.91**	**2.10**

Table 2

Comparison of results to other selected papers. The median values were used from this work.

Source	Animal	Target	μ_{Dias} (kPa)	μ_{Sys} (kPa)	Ratio
Bouchard et al.	Canine t al.	LVFW	0.69	4.00	5.81
Couade et al.	Sheep t al.	LVFW	2.10	23.04	10.96
Pernot et al.	t al. Rat	LVFW	1.21	8.41–12.25	6.95–10.12
Pislaru et al.	tPig al.	RVFW	1.7	31.0	18.23
Kolipaka et al.	Pig t al.	LV	5.76	12.25	2.13
Kanai	Human	IVS		16.00–30.25	
Pig 1	Pig	IVS	1.21	16.24	13.42
Pig 2	Pig	IVS	3.28	23.04	7.03
Pig 3	Pig	IVS	4.84	26.42	5.46
Pig 4	Pig	IVS	1.23	8.64	7.02
Pig 5	Pig	IVS	0.79	6.76	8.53
Pig 6	Pig	IVS	2.31	10.11	4.38